Delft University of Technology

Shallow and Undoped Germanium Quantum Wells
A Playground for Spin and Hybrid Quantum Technology

Sammak, Amir; Sabbagh, Diego; Hendrickx, Nico W.; Lodari, Mario; Paquelet Wuetz, Brian; Tosato, Alberto; Yeoh, La Reine; Veldhorst, Menno; Scappucci, Giordano; More Authors

DOI
10.1002/adfm.201807613

Publication date
2019

Document Version
Final published version

Published in
Advanced Functional Materials

Citation (APA)
Sammak, A., Sabbagh, D., Hendrickx, N. W., Lodari, M., Paquelet Wuetz, B., Tosato, A., Yeoh, L. R., Veldhorst, M., Scappucci, G., & More Authors (2019). Shallow and Undoped Germanium Quantum Wells: A Playground for Spin and Hybrid Quantum Technology. *Advanced Functional Materials*, *29*(14), Article 1807613. https://doi.org/10.1002/adfm.201807613

Important note
To cite this publication, please use the final published version (if applicable).
Please check the document version above.

Copyright
Other than for strictly personal use, it is not permitted to download, forward or distribute the text or part of it, without the consent of the author(s) and/or copyright holder(s), unless the work is under an open content license such as Creative Commons.

Takedown policy
Please contact us and provide details if you believe this document breaches copyrights.
We will remove access to the work immediately and investigate your claim.

This work is downloaded from Delft University of Technology.
For technical reasons the number of authors shown on this cover page is limited to a maximum of 10.

ADVANCED FUNCTIONAL MATERIALS
www.afm-journal.de

Shallow and Undoped Germanium Quantum Wells: A Playground for Spin and Hybrid Quantum Technology

*Amir Sammak, Diego Sabbagh, Nico W. Hendrickx, Mario Lodari, Brian Paquelet Wuetz, Alberto Tosato, LaReine Yeoh, Monica Bollani, Michele Virgilio, Markus Andreas Schubert, Peter Zaumseil, Giovanni Capellini, Menno Veldhorst, and Giordano Scappucci**

Buried-channel semiconductor heterostructures are an archetype material platform for the fabrication of gated semiconductor quantum devices. Sharp confinement potential is obtained by positioning the channel near the surface; however, nearby surface states degrade the electrical properties of the starting material. Here, a 2D hole gas of high mobility (5×10^5 cm^2 V^{-1} s^{-1}) is demonstrated in a very shallow strained germanium (Ge) channel, which is located only 22 nm below the surface. The top-gate of a dopant-less field effect transistor controls the channel carrier density confined in an undoped Ge/SiGe heterostructure with reduced background contamination, sharp interfaces, and high uniformity. The high mobility leads to mean free paths ≈ 6 µm, setting new benchmarks for holes in shallow field effect transistors. The high mobility, along with a percolation density of 1.2×10^{11}cm^{-2}, light effective mass ($0.09m_e$), and high effective *g*-factor (up to 9.2) highlight the potential of undoped Ge/SiGe as a low-disorder material platform for hybrid quantum technologies.

1. Introduction

Germanium (Ge) has the highest hole mobility of common semiconductors and is integrated onto silicon (Si) substrates within a foundry-qualified process.[1] These properties make high-speed Ge transistors appealing for extending chip performance in classical computers beyond the limits imposed by miniaturization. Ge is also emerging as a promising material for quantum technology as it contains crucial parameters for semiconducting, superconducting, and topological quantum electronic devices. The high mobility of holes and their low effective mass promote the confinement of spins in low-disorder Ge quantum dots by uniform potential landscapes.[2] Holes in Ge have large and tunable *g*-factors, with inherent strong spin–orbit interaction. These properties facilitate fast all-electrical qubit control,[3] qubit coupling at a distance via superconductors,[4] and are key ingredients for the emergence of Majorana zero modes for topological quantum computing.

Like Si, Ge can be isotopically purified into a nuclear spin-free material to achieve long spin lifetimes.[5] In contrast, virtually every metal on Ge, including superconductors with high critical fields, show a Fermi level pinned close to the valence band.[6] This facilitates the injection of holes and thus the formation of ohmic superconductor/semiconductor contacts, a key building block in hybrid quantum devices.

These enticing prospects have motivated the theoretical framework for Ge-based spin qubits[7] and Majorana fermions.[8] Experimental milestones in self-assembled Ge nanostructures include gate-tunable superconductivity in Ge/Si nanowires[9] and the demonstration of electrically driven spin qubits[3] and single-shot readout of single spins[10] in Ge hut wires.

Recently, Ge/SiGe heterostructures have emerged as a planar technology that can bring together low disorder, potential for fast qubit driving, and avenue for scaling due to the compatibility with large scale manufacturing. In Ge/SiGe, the band-edge profiles between compressively strained Ge and relaxed Ge-rich $Si_{1-y}Ge_y$ (**Figure 1**; star, $y \approx 0.8$) produce a type I band alignment.[11] This is different from Si/SiGe heterostructures (Figure 1; circle, $y \approx 0.3$) and Ge/Si core–shell nanowires (Figure 1; triangle), where a type II band alignment promotes confinement of either electrons or holes, respectively. Charge carriers can populate the quantum well either by doping the heterostructure or via top

Dr. A. Sammak, Dr. D. Sabbagh, N. W. Hendrickx, Dr. M. Lodari, B. Paquelet Wuetz, A. Tosato, Dr. L. Yeoh, Dr. M. Veldhorst, Dr. G. Scappucci
QuTech and Kavli Institute of Nanoscience
TU Delft, P.O. Box 5046, 2600 GA Delft, The Netherlands
E-mail: g.scappucci@tudelft.nl

Dr. A. Sammak
QuTech and TNO
Stieltjesweg 1, 2628 CK Delft, The Netherlands

Dr. M. Bollani
IFN-CNR
LNESS
Via Anzani 42, 22100 Como, Italy

Dr. M. Virgilio
Dipartimento di Fisica "E. Fermi"
Università di Pisa
Largo Pontecorvo 3, 56127 Pisa, Italy

Dr. M. A. Schubert, Dr. P. Zaumseil, Prof. G. Capellini
IHP
Im Technologiepark 25, 15236 Frankfurt, Germany

Prof. G. Capellini
Dipartimento di Scienze
Università degli studi Roma Tre
Viale Marconi 446, 00146 Roma, Italy

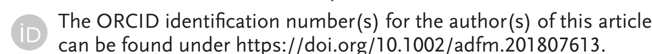
The ORCID identification number(s) for the author(s) of this article can be found under https://doi.org/10.1002/adfm.201807613.

© 2019 The Authors. Published by WILEY-VCH Verlag GmbH & Co. KGaA, Weinheim. This is an open access article under the terms of the Creative Commons Attribution-NonCommercial-NoDerivs License, which permits use and distribution in any medium, provided the original work is properly cited, the use is non-commercial and no modifications or adaptations are made.

The copyright line was changed on 31 January 2019 after initial publication.

DOI: 10.1002/adfm.201807613

© 2019 The Authors. Published by WILEY-VCH Verlag GmbH & Co. KGaA, Weinheim

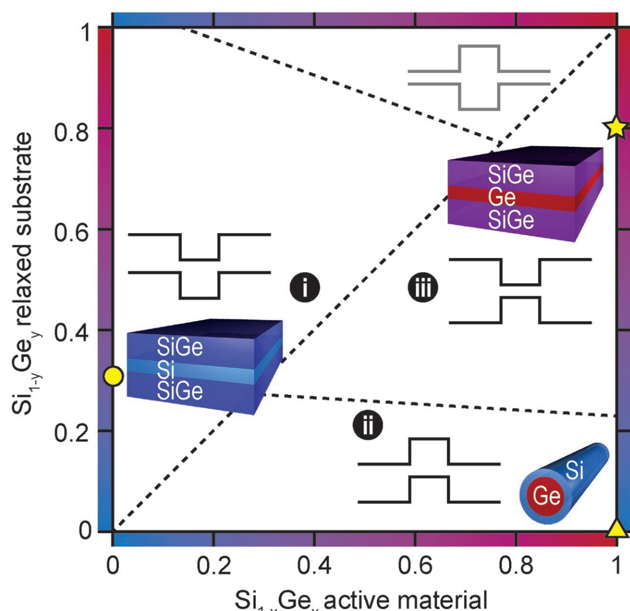

Figure 1. Schematics of SiGe heterostructures band-edge profiles as a function of the Ge concentration *x* and *y* in the active material and in the relaxed substrate, respectively. Star, circle, and triangle refer to Ge/SiGe, Si/SiGe, and Ge/Si heterostructures, respectively. Adapted from ref. [11]

gating. Holes confined in modulation doped Ge/SiGe have shown exceptionally high mobility of 1.5 million $cm^2\ V^{-1}\ s^{-1}$, strong spin–orbit coupling,[12] large effective *g*-factors,[13] and fractional quantum Hall physics.[14] A very light effective mass of $0.055m_e$[15] was measured in Hall-bar devices aligned with the ⟨110⟩ crystallographic direction, further reduced to $0.035m_e$ for the ⟨100⟩ direction.

However, ionized impurities in the doped supply layer are a major source of scattering, charge noise, leakage, and instability for the low-temperature operation of quantum devices.[16] In analogy to electron spin qubits in Si/SiGe,[17] to fabricate gated Ge quantum devices it is preferable to completely eliminate dopant atoms from the Ge/SiGe heterostructure. Indeed, gate controlled quantum dots,[2] ballistic 1D channels,[18] and ballistic phase coherent superconductivity[19] were demonstrated recently by using undoped Ge/SiGe. So far the added complexity in developing reliable gate-stacks has limited the investigation of quantum transport properties in undoped Ge/SiGe to devices with mobilities significantly inferior compared to modulation-doped structures.[20–23]

In this paper, we demonstrate state-of-the-art, very shallow, undoped Ge/SiGe heterostructures and devise a process for fabricating dopant-less heterostructure field effect transistors (H-FETs) without compromising on material quality. The capacitively induced 2D hole gas (2DHG) is positioned only 22 nm below the surface and is therefore suitable for further nanofabrication of well-defined quantum devices.[2] A comprehensive investigation of key electrical properties, such as carriers mobility, critical density for conduction, effective mass, and effective *g*-factor, establishes undoped Ge/SiGe as a promising platform for future hybrid quantum technologies.

2. Results

2.1. Ge/SiGe Heterostructures

Figure 2 shows a schematic of the investigated undoped Ge/SiGe heterostructure along with the results of structural characterization to elucidate the crystallographic, morphological, and chemical properties of the stack.

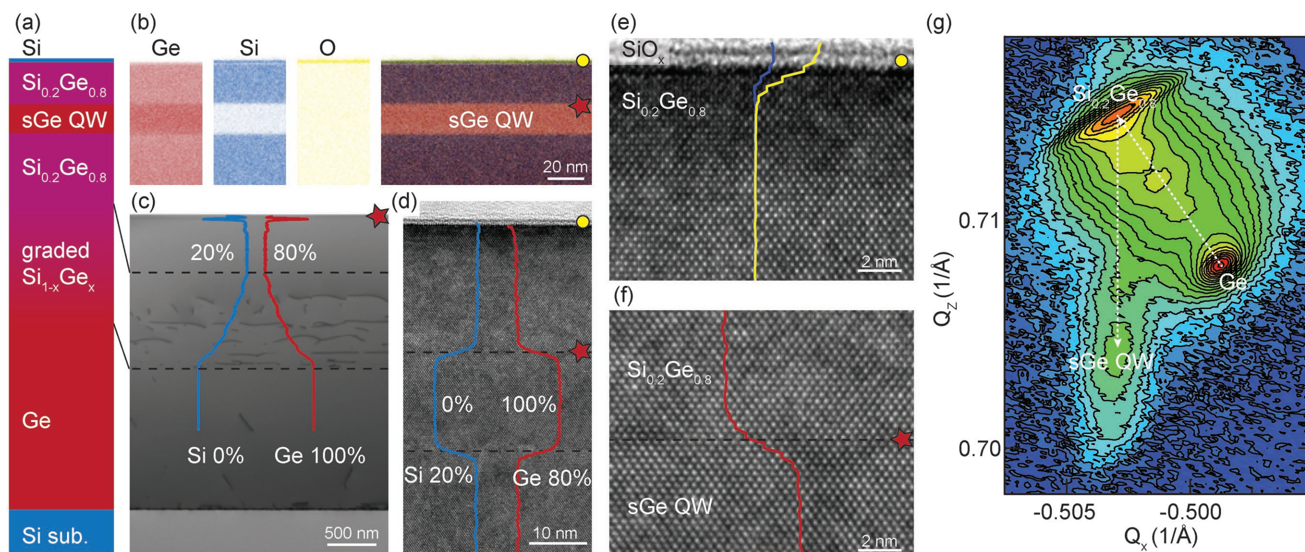

Figure 2. Structural characterization of a Ge/SiGe heterostructure. a) Layer schematics. b) Ge, Si, and O signals from scanning transmission electron microscopy with energy dispersive X-ray analysis (STEM/EDX) of the Ge quantum well and nearby $Si_{0.2}Ge_{0.8}$. c) STEM of the heterostructure with Si and Ge concentration profiles by SIMS. d–f) TEM images showing quantum well/barrier interface (red star) and barrier/surface interface (yellow circle). Superimposed concentration profiles are measured by STEM/EDX. g) X-ray diffraction reciprocal space map of (−2−24) reflection.

© 2019 The Authors. Published by WILEY-VCH Verlag GmbH & Co. KGaA, Weinheim

The Ge/SiGe heterostructure is grown on a 100 mm Si(001) substrate in a high-throughput reduced-pressure chemical vapor deposition reactor (RP-CVD). The layer sequence comprises a $Si_{0.2}Ge_{0.8}$ virtual substrate obtained by reverse grading,[24,25] a 16 nm thick Ge quantum well, a 22 nm thick $Si_{0.2}Ge_{0.8}$ barrier, and a thin sacrificial Si cap (see the Experimental Section). Compared to previous designs of Ge/SiGe stacks,[22] the purpose of the additional Si cap is to provide a well-known starting surface for subsequent high-κ metal gate-stack deposition[26] and to possibly achieve a superior dielectric interface than what SiGe could offer. Secondary ion mass spectroscopy (SIMS) shows a constant oxygen concentration of 2×10^{17} cm^{-3} within the SiGe regions surrounding the quantum well (see the Supporting Information). However, by carefully engineering the growth temperature profile, both carbon and oxygen concentration within the quantum well are below the SIMS detection limit of 4×10^{16} and 8×10^{16} cm^{-3}, respectively, pointing to a very low impurity background level.

Figure 2c highlights the crystalline quality of the $Si_{0.2}Ge_{0.8}$ virtual substrate. The Si and Ge concentration profiles across the virtual substrate (Figure 2c; blue and red curves respectively) confirm the achievement of linear reverse-graded SiGe with targeted alloy composition. Defects and dislocations are confined to the lower layers, at the Si/Ge interface and in the graded $Si_{1-y}Ge_y$. As the Si (Ge) concentration in the SiGe alloy is increased (decreased), relaxation of the upper layers is promoted. By performing preferential etching (see the Experimental Section), we estimate an upper bound for the threading dislocation density of $(3.0 \pm 0.5) \times 10^7$ cm^{-2} for the $Si_{0.2}Ge_{0.8}$.

In-plane and out-of-plane lattice parameters are obtained from the X-ray diffraction reciprocal space map (XRD-RSM) in Figure 2g. The Ge and $Si_{0.2}Ge_{0.8}$ buffer layers are over-relaxed compared to the Si substrate with a residual tensile strain of $\varepsilon_{\parallel} = 0.2\%$ and 0.26%, respectively. This is typical in SiGe virtual substrates due to the difference in thermal contraction of the materials after cooling from the high growth temperature.[24,27] The peak corresponding to the Ge quantum well is vertically aligned to the peak of the $Si_{0.2}Ge_{0.8}$ buffer layer, indicating a pseudomorphic growth of the quantum well and resulting in an in-plane compressive strain of $\varepsilon_{\parallel} = -0.63\%$.

Figure 2b shows the individual and combined signals of Si, Ge, and O from the strained Ge quantum well embedded between $Si_{0.2}Ge_{0.8}$. The Ge quantum well appears as a uniform layer of constant thickness and with sharp interfaces to the adjacent $Si_{0.2}Ge_{0.8}$. The increasing O and Si signals at the top of the heterostructure indicate that the Si cap has readily oxidized upon exposure to air. The absence of extended defects in the high resolution transmission electron microscopy (TEM) images in Figure 2d–f indicates high crystalline quality in the quantum well and adjacent $Si_{0.2}Ge_{0.8}$. The high degree of control achieved in the deposition process results in the Si and Ge composition profiles in Figure 2d–f, with constant Ge composition within each layer of the $Si_{0.2}Ge_{0.8}$/Ge/$Si_{0.2}Ge_{0.8}$ structure. By fitting the scanning transmission electron microscopy with energy dispersive X-ray analysis (STEM/EDX) Ge concentration profile in Figure 2f with an error function,[28,29] we infer that the top interface of the quantum well is abrupt and characterized by a distance $\lambda \leq 0.8$ nm for transitioning between Ge and SiGe (see the Supporting Information).

2.2. Heterostructure Field Effect Transistors

Hall-bar shaped H-FETs oriented along the ⟨110⟩ crystallographic directions were fabricated to investigate the magnetotransport properties of the undoped Ge/SiGe. An external electric field is applied to the insulated top-gate thereby populating the Ge quantum well and creating a 2D hole gas. Compared to undoped Si/SiGe H-FETs,[30] we adopted a low-thermal budget, implantation-free process to obtain direct contact between diffused Pt metallic ohmics and the induced 2DHG (see the Experimental Section). This approach is possible due to the very low platinum germanosilicide hole Schottky barrier height.[31,32]

The optical image of the final device is displayed in **Figure 3** b, together with the schematics of the transistor cross-section

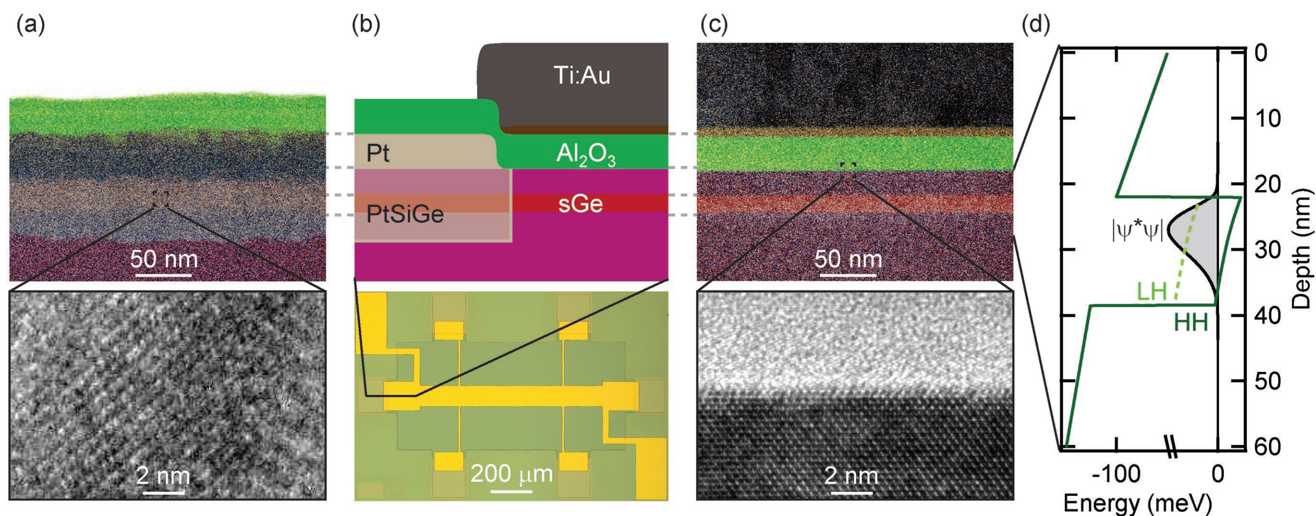

Figure 3. Ge/SiGe heterostructure field effect transistor. a) STEM/EDX (top) and TEM (bottom) in the ohmic contact region. b) Device cross-section schematics and optical image (upper and lower panels, respectively). c) STEM/EDX (top) and TEM (bottom) in the channel region. d) Band-structure simulation with heavy holes (HH), light holes (LH), and charge distribution in the first subband (|ψ*ψ|).

© 2019 The Authors. Published by WILEY-VCH Verlag GmbH & Co. KGaA, Weinheim

at the gate/ohmic contact overlap region. The upper panels in Figure 3a,c show STEM/EDX analysis in the ohmic contact region and under the top-gate, respectively. In the ohmic region (Figure 3a, top panel) Pt diffuses inside the SiGe barrier and surpasses the quantum well. A platinum germanosilicide alloy is formed, with a Ge concentration less than the value of 0.8 present in the as-grown material, due to the Pt dilution within. The formation of a platinum germanosilicide alloy is also supported by the presence of crystalline grains, as visible by TEM (Figure 3a, bottom panel). Since Pt diffusion is achieved at significantly lower temperature than the quantum well growth—300 °C versus 500 °C, respectively—the crystalline quality of the heterostructure under the gate-stack is preserved. The critical Ge/SiGe interfaces after device processing (Figure 3c, top panel) are as sharp as in the as-grown material (Figure 2c). Furthermore, the high-resolution TEM image in the bottom panel of Figure 3c highlights the atomically flat semiconductor/oxide interface.

Figure 3d shows the band-structure in the H-FET at a carrier density of 1×10^{11} cm^{-2} by solving the Schroedinger–Poisson equation as a function of the applied electric field at low temperatures. States in the quantum well with heavy hole (HH) symmetry are favored compared to light holes (LH) states, with the HH and LH band-edges split in energy by 40 meV. The wavefunction of the fundamental HH state is well confined in the Ge quantum well, with an energy splitting between the fundamental HH state and the fundamental LH state of 47 meV, and between the fundamental and the first excited HH state of 15 meV. These obtained energy splittings in Ge/SiGe are more than one order of magnitude larger than the valley splitting in the conduction band of Si/SiGe or Si/SiO_2 systems,[33] supporting the possibility of obtaining well defined qubits in this material platform.

2.3. Mobility, Critical Density, and Effective Mass

Magnetotransport characterization of the Ge/SiGe H-FET was performed at low temperatures to elucidate the quantum transport properties of the 2DHG. The device is operated in accumulation mode, in which carriers populate the undoped quantum well by applying a negative DC voltage bias (V_g) to the top-gate (relative to the drain contact). Upon applying a fixed AC voltage bias to source and drain contacts (V_{sd}), standard four-probe lock-in techniques allow to measure the longitudinal and transverse components of the resistivity tensor (ρ_{xx} and ρ_{xy}, respectively), from which longitudinal (σ_{xx}) and transverse (σ_{xy}) conductivity are extracted. The active carrier density p_{2D} is measured by the Hall effect and, consequently, the carrier mobility μ (see the Experimental Section).

Figure 4 a shows the conductivity and the carrier density as a function of gate voltage (blue and black curves, respectively).

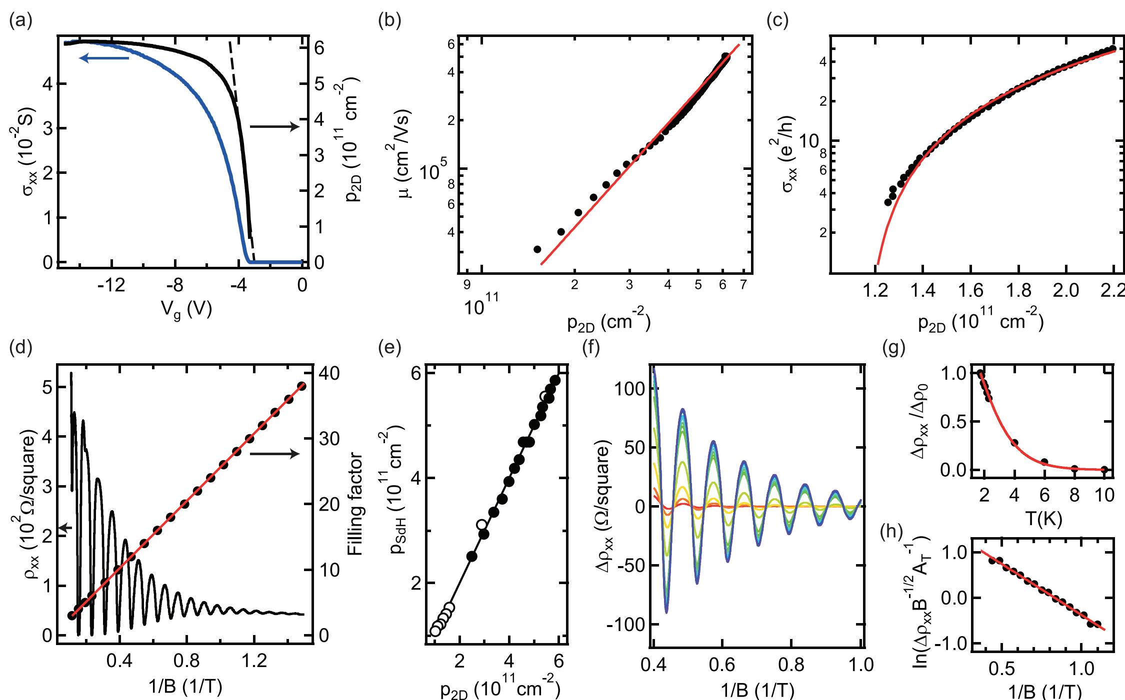

Figure 4. Transport measurements at $T = 1.7$ K as a function of magnetic field B and carrier density p_{2D}. a) Conductivity σ_{xx} (blue line) and Hall density p_{2D} (black line) as a function of gate voltage V_g at 1.7 K. Dashed line is a linear fit of the gate-dependent density at low V_g. b) Density-dependent mobility μ (solid circles) and power law fit (red curve). c) Density-dependent σ_{xx} (solid circles) and fit to percolation theory (red line). d) Magnetoresistivity ρ_{xx} (black line) and filling factor (solid circles) at saturation density as a function of inverse magnetic field $1/B$. Red line is the fit to the filling factor progression. e) Density p_{SdH} obtained by the analysis of the Shubnikov–de Haas oscillations plotted against the corresponding Hall density p_{2D}. Open and solid circles are measured at 1.7 K and 50 mK, respectively. f) Temperature dependence of the Shubnikov–de Haas oscillations $\Delta\rho$ in the range $T = 1.7$–10 K, after background subtractions. g) $\Delta\rho$ (solid circles) as a function of T, normalized at $\Delta\rho_0 = \Delta\rho(T_0 = 1.7\,K)$. The red line is the fit used to extract m^*. h) Dingle plot at $T_0 = 1.7$ K (see the Experimental Section). The red line is the linear fit used to extract τ_q.

© 2019 The Authors. Published by WILEY-VCH Verlag GmbH & Co. KGaA, Weinheim

At zero applied V_g there are no carriers induced in the quantum well, the undoped heterostructure is insulating and, as expected, no conduction is measured. Above a threshold bias (V_g = −3.8 V), current starts flowing in the channel and σ_{xx} increases monotonically until saturation. After turn-on of the capacitively induced 2DHG, p_{2D} increases linearly as V_g sweeps more negative. This is consistent with a simple parallel-plate capacitor model in which the $Si_{0.2}Ge_{0.8}$ and Al_2O_3 layers are the dielectric layers between the Ge quantum well and the metallic top-gate. The extracted effective gate capacitance obtained by fitting the linear portion of the p_{2D} versus V_g curve, however, is reduced to ≈60% of the expected value. At larger V_g the p_{2D} versus V_g curve deviates from linearity and eventually p_{2D} saturates at a value of 6×10^{11} cm^{-2}.

Figure 4b shows the density-dependent mobility. The mobility increases strongly with density over the entire range of accessible densities, without signs of saturation. By fitting the data to a power law dependence $\mu = p_{2D}^{\alpha}$, we find a large exponent $\alpha = 2.1$. Including local field corrections,[34,35] exponents $\alpha \geq 1.5$ indicate that the mobility is still limited by scattering from remote impurities at the dielectric/semiconductor interface, as seen previously in Si/SiGe heterostructures.[20,36] At saturation density $p_{2D} = 6 \times 10^{11}$ cm^{-2} we measure a maximum mobility of 5×10^5 cm^2 V^{-1} s^{-1}, corresponding to a mean free path of ≈6 µm, setting new benchmarks for holes in shallow H-FET devices.

The critical density for establishing metallic conduction in the channel is extracted by fitting the density-dependent conductivity (Figure 4c) in the low density regime to percolation theory[37,38] $\sigma_{xx} \propto (p_{2D} - p_p)^p$ cm^{-2}. By fixing the exponent $p = 1.31$, as expected in a 2D system, we estimate a percolation threshold density $p_p = 1.15 \times 10^{11}$ cm^{-2} at 1.7 K, which sets an upper bound for p_p at the temperature at which qubits typically operate ($T \leq 100$ mK). Note that this value is in agreement with the qualitative estimate of critical density $p_c = 1.19 \times 10^{11}$ cm^{-2} obtained by extrapolating to zero the linear region of mobility µ versus log(p_{2D}) curve.[39] The obtained percolation threshold density is similar to the values reported in high quality Si metal-oxide semiconductor field-effect transistor,[37,38] and ≈ 2× higher than the values reported in undoped Si/SiGe,[30] possibly because the dielectric interface in our samples is much closer to the channel (22 nm compared to 50 nm in ref. [30]).

Figure 4d shows the Shubnikov–de Haas (SdH) oscillations in the magnetoresistivity at saturation density. The oscillations minima reach zero value at high magnetic field B and are periodic against $1/B$. From the linear filling factor progression (Figure 4d, red circles) we extract a density $p_{SdH} = 6.1 \times 10^{11}$ cm^{-2}, in agreement with the Hall data. The agreement $p_{SdH} = p_{2D}$ is verified throughout the range of investigated density and temperature (Figure 4e). Figure 4f shows the temperature dependent magnetoresistance oscillation amplitude $\Delta\rho$ at a density $p_{2D} = 5.4 \times 10^{11}$ cm^{-2} as a function of the inverse of $1/B$, after the subtraction of a polynomial background. The hole effective mass m^* is extracted by fitting the damping of the SdH oscillation amplitude with increasing temperature at B = 1.4 T (Figure 4g, see the Experimental Section). The obtained value $m^* = (0.090 \pm 0.002)m_e$, where m_e is the free electron mass, is comparable to previous reports in Ge/SiGe at similar densities.[20,23] The quantum lifetime τ_q at 1.7 K is extracted by fitting the SdH oscillation envelope.[40] From the Dingle plot in Figure 4h, we estimate τ_q = 0.74 ps, corresponding to a large Dingle ratio $\tau_t/\tau_q = 27$, where τ_t is the transport lifetime. The obtained large Dingle ratio confirms that the mobility is limited by scattering from charges trapped at the dielectric/heterostructure interface.

2.4. Landau Fan Diagram and Effective *g*-Factor.

In **Figure 5** a,b, we show color plots of ρ_{xx} as well as the transversal Hall signal σ_{xy} at T = 50 mK, as a function of out-of-plane magnetic field B and carrier density p_{2D}, as obtained from the low-field Hall data. In this Landau fan diagram, both the quantum Hall effect (Figure 5a) and SdH oscillations (Figure 5b) fan out linearly toward higher field and density. As in the measurements at 1.7 K (Figure 4f), we do not observe beatings in the SdH oscillations. This prevents us from directly measuring the strength of the spin–orbit interaction. However, we estimate an upper bound for spin-splitting in the 2DHG of 1.5 meV from the peak width of 1.5 T^{-1} observed in the Fourier transform of ρ_{xx} against $1/B$. Observation of a Landau fan diagram of such quality is a sign of the very low disorder in the 2D channel. These measurements allow to estimate the out-of-plane effective g-factor (g^*) by comparing the field strength B_L at which SdH

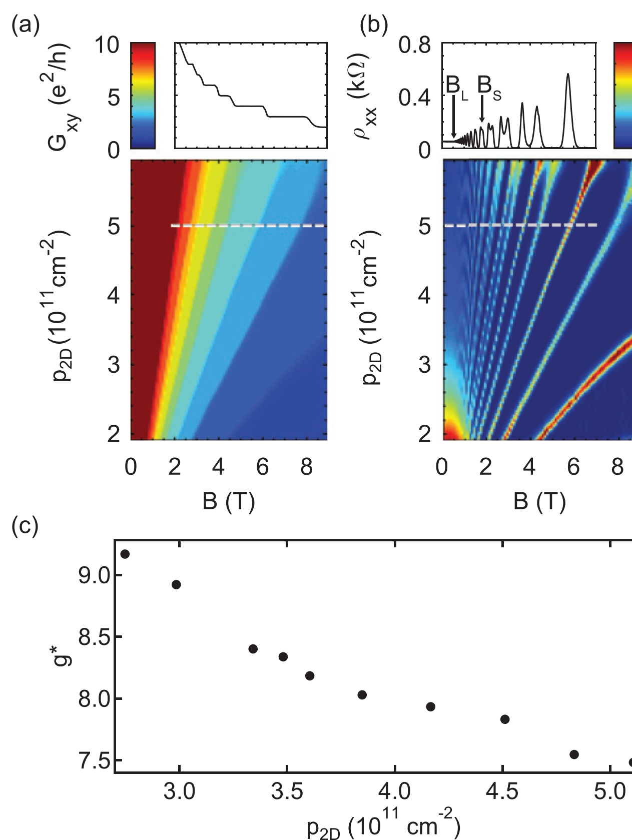

Figure 5. Transport measurements at T = 50 mK as a function of magnetic field B and carrier density p_{2D}. a) Quantized Hall conductance and b) Shubnikov–de Haas oscillations. B_L and B_S mark the magnetic field at which Shubnikov–de Haas oscillations and Zeeman splitting are resolved, respectively. c) Effective g-factor as a function of density.

© 2019 The Authors. Published by WILEY-VCH Verlag GmbH & Co. KGaA, Weinheim

oscillations appear in Figure 5b to the field B_S at which the spin-splitting occurs[30] as a function of density (see the Experimental Section). We observe in Figure 5c a decrease of $\langle g^* \rangle$ from ≈9.2 to ≈7.5 with increasing density. We attribute such decrease to a higher degree of admixture of the light hole states at higher densities, due the nonparabolicity of the valence band.[13]

3. Discussion

The observed $p_{2D} - V_g$ and $\mu - p_{2D}$ dependences are in line with previous studies on shallow undoped Si and Ge/SiGe heterostructures.[22,41] At small electric fields, carrier tunneling can occur from the shallow Ge quantum well to defect states in the bandgap of the dielectric/SiGe interface. While tunneling reduces the gate capacitance, the passivation of the surface impurities by tunneled carriers also lead to an enhanced mobility.[42] We speculate that this mechanism is causing the observed upturn in the $\mu - p_{2D}$ dependence above a density of $p_{2D} = 3 \times 10^{11}$ cm^{-2}, as described in ref. [41]. At higher electric fields, the Fermi level aligns with the valence band-edge at the dielectric/SiGe interface. Population of the surface quantum well prevents, by screening, further carrier accumulation in the buried channel, which reaches saturation. Nevertheless, only the buried quantum well contributes to transport, since the surface quantum well carrier concentration is likely below the mobility edge threshold, which is typically high for a channel at the Al_2O_3/Si interface. This interpretation is supported by the matching densities p_{2D} and p_{SdH} (Figure 4d), with no beating observed in the SdH oscillations: only one high mobility subband contributes to the measured transport.

In conclusion, by measuring key transport metrics at low temperatures, we have shown that shallow and undoped Ge/SiGe heterostructures are a promising low-disorder platform for Ge quantum devices. The reported half-million mobility sets new benchmarks for Si and Ge shallow-channel H-FETs,[22,41,42] while even higher mobilities may be obtained by further improving the semiconductor/dielectric interface. Possible avenues in these directions include the removal of the native silicon oxide layer prior to high-κ dielectric deposition and/or postmetallization thermal anneals. A better quality semiconductor/dielectric interface should also improve the critical density, which is a crucial metric for quantum devices.

The measured hole effective mass of $0.09m_e$ is much lighter than the corresponding value for electrons in silicon ($0.19m_e$) and is close to the one featured by conduction carriers in GaAs ($0.067m_e$). A lighter effective mass is beneficial for spin qubits since it not only corresponds to larger energy level spacing in quantum dots, but also allows to relax lithographic fabrication requirements thanks to a larger extent of the wavefunction. Notice that an even lighter value of about $0.05m_e$,[7] should be within reach for undoped Ge/SiGe, upon improving the semiconductor/dielectric interface or alternatively increasing the distance separating the quantum from the interface. In fact, in both the cases, a lower 2D hole density regime can be accessed[20]; since it is known that nonparabolicity effects tend to increase the effective mass,[43] it follows that smaller values are to be expected due to the decreasing of the Fermi vector associated to lower hole densities.

4. Experimental Section

Heterostructure Growth: The Ge/SiGe heterostructure was grown in an RP-CVD reactor (ASMI Epsilon 2000) in one deposition cycle using germane (GeH_4) and dichlorosilane (SiH_2Cl_2) as precursor gases. Starting with a 100 mm Si(001) substrate, a 1.4 µm thick layer of Ge was grown using a dual-step process. An initial low-temperature (400 °C) growth of a Ge seed layer was followed by a higher temperature (625 °C) overgrowth of a thick relaxed Ge buffer layer. Cycle anneals at 800 °C were performed to promote full relaxation of the Ge. The subsequent 900 nm thick reverse-graded $Si_{1-y}Ge_y$ layer[24] was grown at 800 °C with y changing from 1 to 0.8. The SiGe virtual substrate was completed by a $Si_{0.2}Ge_{0.8}$ buffer layer of uniform composition, which was initially grown at 800 °C. For the final 160 nm, the growth temperature was lowered to match the growth temperature of the subsequent layers (500 °C). In this way, growth interruption for temperature equilibration was avoided at the critical quantum well/virtual substrate interface. The heterostructure was completed with the deposition of a 16 nm thick Ge quantum well, a 22 nm thick $Si_{0.2}Ge_{0.8}$ barrier, and a thin (<2 nm) sacrificial Si cap.

Structural Analysis: X-ray diffraction measurements were performed with a 9 kW SmartLab diffractometer from Rigaku equipped with a Ge(400 × 2) crystal collimator and a Ge(220 × 2) crystal analyzer using CuK1 radiation. The asymmetric (−2−24) reflection was used for reciprocal space mapping to determine in-plane and out-of-plane lattice parameters. Transmission electron microscope investigation was carried out using a FEI Tecnai Osiris. For EDX, the TEM was operated in STEM mode. The beam energy for all TEM measurements was 200 keV. Preferential etching techniques were used to estimate upper bounds for threading dislocation density in the SiGe virtual substrate. A solution of 10 mL HF (50% vol) + 15 mL HNO_3 (69% vol) + 1 mg KI + 1 mg I_2 + 5 mL CH_3COOH (100%vol) + 60 mL H_2O was employed for 6 s at a temperature of 273 K. Counting statistics was performed on SiGe etched surfaces imaged by atomic force microscopy.

Device Fabrication: The process for undoped Ge/SiGe H-FETs comprised the deposition of metallic ohmics, high-κ dielectric, and metallic top-gate. Ohmic pads were deposited on top of a mesa structure by e-beam evaporation of 60 nm of Pt. An HF dip was performed prior Pt deposition to etch the native oxide at the surface and ensure that the Pt film is in direct contact with the underlying $Si_{0.2}Ge_{0.8}$. The subsequent atomic layer deposition of 30 nm of Al_2O_3 at 300 °C has the twofold purpose of electrically isolating the transistors top-gate from the channel as well as providing the thermal budget needed to drive the Pt ohmics in the $Si_{0.2}Ge_{0.8}$. Finally, the top-gate was realized by depositing 10/150 nm of Ti/Au.

Electrical Measurements: Magnetotransport data in the temperature range of 1.7–10 K were obtained in a ^{4}He refrigerator equipped with a variable temperature insert and a 9 T magnet. Magnetotransport data at 50 mK were obtained in a ^{3}He dilution refrigerator equipped with a 9 T magnet. A bias in the 0.1–1 mV range, frequency 7.7 Hz, was applied to the source and drain contacts. The source–drain current I_{sd}, the longitudinal voltage V_{xx}, and the transverse Hall voltage V_{xy} were measured; the longitudinal resistivity ρ_{xx} and transverse Hall resistivity ρ_{xy} were calculated as $\rho_{xx} = V_{xx}/I_{sd} \times W/L$ and $\rho_{xy} = V_{xy}/I_{sd}$, respectively (aspect ratio $L/W = 5$). Longitudinal (σ_{xx}) and transverse (σ_{xy}) conductivity were calculated from ρ_{xx} and ρ_{xy} by tensor inversion. The electrically active Hall carrier density p_{2D} was obtained from the linear dependence of the Hall resistivity with perpendicular magnetic field ($\rho_{xy} = B/ep_{2D}$) at low magnetic field values ($B \leq 0.5$ T). The carrier mobility µ was obtained from the relationship $1/\rho_{xx} = p_{2D}e\mu$. The effective mass m^* was fitted from the damping of the SdH oscillations by using the expression[44]

$$\frac{\Delta\rho_{xx}}{\Delta\rho_0} = \frac{\Delta\rho/\rho_0(T)}{\Delta\rho/\rho_0(T_0)} = \frac{A_T}{A_{T_0}} = \frac{T\,\sinh(\alpha T_0)}{T_0\,\sinh(\alpha T)} \quad (1)$$

where $\alpha = \frac{2\pi k_B m^*}{\hbar e B}$, k_B is Boltzmann constant, $\hbar$ is the Planck constant, ρ_0 is the zero-field resistivity, and $T_0 = 1.7$ K is the coldest temperature at which the oscillations were measured. Estimation of the effective g-factor g^* (Figure 5c) was performed as following. For a magnetic

© 2019 The Authors. Published by WILEY-VCH Verlag GmbH & Co. KGaA, Weinheim

field strength B_L, Shubnikov–de Haas oscillations begin to be visible and the Landau level spacing minus the Zeeman splitting $\hbar eB_L/m^*-g^*\mu_B B_L$ equals the Landau level broadening $\Gamma(B_L)$. Here μ_B is the Bohr magneton. For a magnetic field strength B_S, the first Zeeman spin-splitting is observed and the Zeeman energy $g^*\mu_B B_S$ equals $\Gamma(B_S)$. Taking into account the field dependent broadening of the Landau levels, $\Gamma(B) = C\sqrt{B}$,[45] g^* is described by the relation

$$g^* = \frac{2m_e}{m^*}\frac{1}{1+\sqrt{B_S/B_L}} \qquad (2)$$

Supporting Information

Supporting Information is available from the Wiley Online Library or from the author.

Acknowledgements

A.S. and D.S. contributed equally to this work. The authors acknowledge support through a FOM Projectruimte of the Foundation for Fundamental Research on Matter (FOM), associated with the Netherlands Organisation for Scientific Research (NWO). All data underlying this study are available from the 4TU ResearchData repository at https://doi.org/10.4121/uuid:bbdf6137-18bd-4973-b917-748528cd6637.

Conflict of Interest

The authors declare no conflict of interest.

Keywords

germanium, mobility, quantum devices, quantum well

Received: October 26, 2018
Revised: December 21, 2018
Published online:

[1] R. Pillarisetty, *Nature* **2011**, *479*, 324.
[2] N. W. Hendrickx, D. P. Franke, A. Sammak, M. Kouwenhoven, D. Sabbagh, L. Yeoh, R. Li, M. L. V. Tagliaferri, M. Virgilio, G. Capellini, G. Scappucci, M. Veldhorst, *Nat. Commun.* **2018**, *9*, 2835.
[3] H. Watzinger, J. Kukučka, L. Vukušić, F. Gao, T. Wang, F. Schäffler, J.-J. Zhang, G. Katsaros, *Nat. Commun.* **2018**, *9*, 3902.
[4] C. Kloeffel, M. Trif, P. Stano, D. Loss, *Phys. Rev. B* **2013**, *88*, 241405.
[5] K. M. Itoh, H. Watanabe, *MRS Commun.* **2014**, *4*, 143.
[6] A. Dimoulas, P. Tsipas, A. Sotiropoulos, E. K. Evangelou, *Appl. Phys. Lett.* **2006**, *89*, 252110.
[7] L. Terrazos, A. Saraiva, X. Hu, M. Friesen, S. Coppersmith, B. Koiller, R. B. Capaz, *arXiv:1803.10320*.
[8] F. Maier, J. Klinovaja, D. Loss, *Phys. Rev. B* **2014**, *90*, 195421.
[9] J. Xiang, A. Vidan, M. Tinkham, R. M. Westervelt, C. M. Lieber, *Nat. Nanotechnol.* **2006**, *1*, 208.
[10] L. Vukušić, J. Kukučka, H. Watzinger, J. M. Milem, F. Schäffler, G. Katsaros, *Nano Lett.* **2018**, *18*, 7141.
[11] M. Virgilio, G. Grosso, *J. Phy.: Condens. Matter* **2006**, *18*, 1021.
[12] M. Failla, J. Keller, G. Scalari, C. Maissen, J. Faist, C. Reichl, W. Wegscheider, O. J. Newell, D. R. Leadley, M. Myronov, J. Lloyd-Hughes, *New J. Phys.* **2016**, *18*, 113036.
[13] I. Drichko, A. Dmitriev, V. Malysh, I. Y. Smirnov, H. Von Känel, M. Kummer, D. Chrastina, G. Isella, *J. Appl. Phys.* **2018**, *123*, 165703.
[14] Q. Shi, M. Zudov, C. Morrison, M. Myronov, *Phys. Rev. B* **2015**, *91*, 241303.
[15] C. Morrison, M. Myronov, *Appl. Phys. Lett.* **2017**, *111*, 192103.
[16] M. G. Borselli, K. Eng, E. T. Croke, B. M. Maune, B. Huang, R. S. Ross, A. A. Kiselev, P. W. Deelman, I. Alvarado-Rodriguez, A. E. Schmitz, M. Sokolich, K. S. Holabird, T. M. Hazard, M. F. Gyure, A. T. Hunter, *Appl. Phys. Lett.* **2011**, *99*, 063109.
[17] B. M. Maune, M. G. Borselli, B. Huang, T. D. Ladd, P. W. Deelman, K. S. Holabird, A. A. Kiselev, I. Alvarado-Rodriguez, R. S. Ross, A. E. Schmitz, M. Sokolich, C. A. Watson, M. F. Gyure, A. T. Hunter, *Nature* **2012**, *481*, 344.
[18] R. Mizokuchi, R. Maurand, F. Vigneau, M. Myronov, S. De Franceschi, *Nano Lett.* **2018**, *18*, 4861.
[19] N. Hendrickx, M. Tagliaferri, M. Kouwenhoven, R. Li, D. Franke, A. Sammak, A. Brinkman, G. Scappucci, M. Veldhorst, *arXiv:1808.00763*.
[20] D. Laroche, S.-H. Huang, Y. Chuang, J.-Y. Li, C. W. Liu, T. M. Lu, *Appl. Phys. Lett.* **2016**, *108*, 233504.
[21] T. Lu, C. Harris, S.-H. Huang, Y. Chuang, J.-Y. Li, C. Liu, *Appl. Phys. Lett.* **2017**, *111*, 102108.
[22] Y.-H. Su, Y. Chuang, C.-Y. Liu, J.-Y. Li, T.-M. Lu, *Phys. Rev. Mater.* **2017**, *1*, 044601.
[23] W. J. Hardy, C. Harris, Y.-H. Su, Y. Chuang, J. Moussa, L. Maurer, J.-Y. Li, T.-M. Lu, D. R. Luhman, *arXiv:1808.07077*.
[24] V. A. Shah, A. Dobbie, M. Myronov, D. J. F. Fulgoni, L. J. Nash, D. R. Leadley, *Appl. Phys. Lett.* **2008**, *93*, 192103.
[25] G. Capellini, M. De Seta, Y. Busby, M. Pea, F. Evangelisti, G. Nicotra, C. Spinella, M. Nardone, C. Ferrari, *J. Appl. Phys.* **2010**, *107*, 063504.
[26] B. Vincent, R. Loo, W. Vandervorst, J. Delmotte, B. Douhard, V. K. Valev, M. Vanbel, T. Verbiest, J. Rip, B. Brijs, T. Conard, C. Claypool, S. Takeuchi, S. Zaima, J. Mitard, B. De Jaeger, J. Dekoster, M. Caymax, *Solid-State Electron.* **2011**, *60*, 116.
[27] G. Capellini, M. De Seta, P. Zaumseil, G. Kozlowski, T. Schroeder, *J. Appl. Phys.* **2012**, *111*, 073518.
[28] T. E. Clark, P. Nimmatoori, K.-K. Lew, L. Pan, J. M. Redwing, E. C. Dickey, *Nano Lett.* **2008**, *8*, 1246.
[29] J. T. Held, K. I. Hunter, N. Dahod, B. Greenberg, D. R. Hickey, W. A. Tisdale, U. Kortshagen, K. A. Mkhoyan, *ACS Appl. Nano Mater.* **2018**, *1*, 989.
[30] X. Mi, T. Hazard, C. Payette, K. Wang, D. Zajac, J. Cady, J. Petta, *Phys. Rev. B* **2015**, *92*, 035304.
[31] J. Kittl, K. Opsomer, C. Torregiani, C. Demeurisse, S. Mertens, D. Brunco, M. Van Dal, A. Lauwers, *Mater. Sci. Eng., B* **2008**, *154*, 144.
[32] E. Alptekin, C. J. Kirkpatrick, V. Misra, M. C. Ozturk, *IEEE Trans. Electron Devices* **2009**, *56*, 1220.
[33] F. A. Zwanenburg, A. S. Dzurak, A. Morello, M. Y. Simmons, L. C. Hollenberg, G. Klimeck, S. Rogge, S. N. Coppersmith, M. A. Eriksson, *Rev. Mod. Phys.* **2013**, *85*, 961.
[34] V. Dolgopolov, E. Deviatov, A. Shashkin, U. Wieser, U. Kunze, G. Abstreiter, K. Brunner, *Superlattices Microstruct.* **2003**, *33*, 271.
[35] A. Gold, *J. Appl. Phys.* **2010**, *108*, 063710.
[36] T. Lu, C.-H. Lee, S.-H. Huang, D. Tsui, C. Liu, *Appl. Phys. Lett.* **2011**, *99*, 153510.
[37] L. A. Tracy, E. Hwang, K. Eng, G. Ten Eyck, E. Nordberg, K. Childs, M. S. Carroll, M. P. Lilly, S. D. Sarma, *Phys. Rev. B* **2009**, *79*, 235307.

© 2019 The Authors. Published by WILEY-VCH Verlag GmbH & Co. KGaA, Weinheim

[38] J.-S. Kim, A. M. Tyryshkin, S. A. Lyon, *Appl. Phys. Lett.* **2017**, *110*, 123505.
[39] D. McCamey, M. Francis, J. McCallum, A. Hamilton, A. Greentree, R. Clark, *Semicond. Sci. Technol.* **2005**, *20*, 363.
[40] P. Coleridge, R. Stoner, R. Fletcher, *Phys. Rev. B* **1989**, *39*, 1120.
[41] D. Laroche, S.-H. Huang, E. Nielsen, Y. Chuang, J.-Y. Li, C.-W. Liu, T.-M. Lu, *AIP Adv.* **2015**, *5*, 107106.
[42] C.-T. Huang, J.-Y. Li, K. S. Chou, J. C. Sturm, *Appl. Phys. Lett.* **2014**, *104*, 243510.
[43] T. Irisawa, M. Myronov, O. Mironov, E. Parker, K. Nakagawa, M. Murata, S. Koh, Y. Shiraki, *Appl. Phys. Lett.* **2003**, *82*, 1425.
[44] W. De Lange, F. Blom, J. Wolter, *Semicond. Sci. Technol.* **1993**, *8*, 341.
[45] P. Coleridge, *Solid State Commun.* **2003**, *127*, 777.

 © 2019 The Authors. Published by WILEY-VCH Verlag GmbH & Co. KGaA, Weinheim